

Low palaeopressure of the martian atmosphere estimated from the size distribution of ancient craters

Edwin S. Kite, Jean-Pierre Williams, Antoine Lucas and Oded Aharonson

1. Geologic Constraints and Geologic Context.

1a. Stratigraphic Control.

Stratigraphic relations prove that our DTMs sample near the center of a thick interval of fluvial deposition; therefore, the rivers in our study area do not represent the final gasp of large-river activity. The most recent published map covering Aeolis Dorsa is Zimbelman & Scheidt (2012). Our DTMs straddle the contact of two fluvial units (Fig. S1) within the area mapped by Zimbelman & Scheidt as “AHm1.” These units are traceable for >300 km. The lower of the two units, which we informally term F1 (Fluvial 1), contains broad meander-belts. Material laterally adjacent to channel belts erodes to form yardangs, leaving the meander-belts as locally high-standing features. F1 is overlain, apparently conformably, by F2 (Fluvial 2). The surface trace of this contact intersects both of our DTMs. F2 is a slope-forming, smoothly-eroding unit, densely peppered with rimless craters, interpreted as impact craters. Across Aeolis Dorsa, F2’s observed crater density is higher than that of the units which sandwich it, especially near the contact with F1. F2 is associated with young aeolian bedforms. We interpret the sediment source for these bedforms to be erosion of F2. The erosional expression of channels in F2 is variable, but relative to channels in F1 they are typically narrower, have more frequent confluences, form more tree-like as opposed to subparallel networks, and are less frequently preserved in inverted relief than are channels in F1. F2 is >100m thick and is overlain by additional channel-containing units (not obviously exposed in our DTMs) that feature channel belts wider than those in F2. In all cases, channels show little relationship to the modern topography (e.g. Lefort et al., 2012) and the channels are eroding out of the rock. Because the channels are embedded in the stratigraphy, F2 channels postdate F1 channels. The base of F1 is not exposed near our study region, but it is at least tens of meters below the F1-F2 contact. Because our DTMs sample at/near the base of a thick channel-containing unit that is overlain by further channel-containing units, we conclude that our *P* constraint corresponds to the heart of a major river-forming time interval on Mars (conceivably,

31 the *only* major river-forming time interval on Mars; Howard et al., 2005). The total stratigraphic
32 interval over which fluvial deposits are abundant in Aeolis Dorsa is >300m.

33

34 The simplest interpretation of the interfluvial materials in both F1 and F2 is that they consist of the
35 overbank deposits of rivers, but other interpretations are possible. For example, the river deposits
36 could be the fill of incised valleys that postdate the interfluvial materials.

37

38 **1b. Age Control**

39 The craters date from around the time when large rivers flowed on the surface of Mars; they are
40 almost certainly pre-Amazonian, and probably Early Hesperian or older. We carried out a CTX
41 crater count over an 8.3×10^4 km² region largely coterminous with Aeolis Dorsa (Fig. S2a),
42 categorizing craters > 1km in diameter as ‘postfluvial,’ ‘synfluvial/prefluvial,’ and ‘undetermined’
43 on the basis of local crosscutting relationships. Based on crater morphology we think most of the
44 ‘undetermined’ craters are in fact postfluvial, implying a N(1) Crater-Retention Age (CRA) on the
45 Hesperian/Amazonian boundary and an N(2) CRA straddling the Late Hesperian/Early Hesperian
46 boundary (where N(x) is the frequency of craters with $D > x$ km per 10^6 km² count area; Werner &
47 Tanaka, 2011) (Fig. S2b). Stratigraphic relations (Zimbelman & Scheidt, 2012), buttes that we
48 interpret as outliers of formerly sheet-like stratigraphic units, and the shallower slopes of the
49 diameter-frequency curves (Smith et al., 2008) for craters <2km diameter (Fig. S2b) all strongly
50 suggest removal of several hundreds of meters of overburden. Removal of overburden would also
51 remove craters, so our CRAs are minima. This further supports our inference that the rivers flowed
52 in the Hesperian or Late Noachian. Excluding craters <2 km diameter for which overburden-
53 removal effects are most severe, the nominal ages from `craterstats2` (Michael and Neukum,
54 2010) fits to these data are 3.44 (+0.06/–0.10) Ga for the postfluvial population ($n = 34$; red
55 triangles in Figure 2b), 3.61 (+0.03/–0.04) Ga additionally including the undetermined population
56 (total $n = 52$; blue circles in Figure 2b), and 3.71 (+0.02/–0.03) Ga additionally including
57 synfluvial/prefluvial craters (total $n = 68$; green squares in Figure 2b). These nominal ages adopt
58 the Ivanov (2001) production function (PF) and the Hartmann & Neukum (2001) chronology
59 function (CF).

60

61 Our preferred nominal age for the rivers (postfluvial craters + undetermined craters) is identical to
62 the formation age of Gale crater reported by Le Deit et al. 2013 using the same PF and CF (3.61
63 (+0.04/−0.06) Ga). This suggests that our paleopressure constraint applies to the sedimentary
64 deposits infilling Gale crater, reinflating a thin atmosphere via post-Noachian volcanic degassing is
65 difficult (Stanley et al. 2011).

66

67 Our DTMs lie within a region of Aeolis Dorsa (Figure S2a) that has an unusually low N(1): if this
68 results from relatively rapid exhumation, consistent with the excellent preservation state of the
69 ancient river deposits, a resurfacing rate of $\sim 1 \mu\text{m}/\text{yr}$ is implied over 10^{8-9} yr timescales. Relatively
70 rapid modern erosion, combined with a high embedded-crater density, makes this a particularly
71 attractive site for our procedure. Rapid erosion minimizes the proportion of geologically-recent
72 (synerosional) craters in the crater population, and thus the impact of false positives (assuming that
73 the fraction of young craters falsely classified as ancient is fixed). Our results are consistent with
74 Zimbelman & Scheidt (2012), who additionally suggest that the rivers (i.e. Zimbelman & Scheidt's
75 "AHml1") predate a topographically high-standing unit (their "Hm," surrounding Asau crater)
76 with a ~ 3.7 Ga CRA on the Hartmann & Neukum (2001) chronology. Regional geology as mapped
77 by Irwin & Watters (2010) implies that the rivers are not older than Late Noachian.

78

79 We briefly explain the chronological constraints shown for the other data points in Fig. 3. The
80 prehnite ("2*") age estimate assumes prehnite formation prior to the Isidis impact (Fassett & Head,
81 2011), consistent with although not required by geologic relations (Ehlmann et al. 2011); the
82 carbonate Mg/Ca/Fe ("3*") age estimate assumes that the Comanche outcrop formed after the
83 Gusev impact but prior to the Gusev plains lavas (Greeley et al., 2005); for the $^{40}\text{Ar}/^{36}\text{Ar}$ age
84 constraint ("4*") we use the 4.16 ± 0.04 Ga age adopted by Ref. 31; and for the bomb sag ("5*")
85 age estimate we assume a pre-Amazonian age. All of these ages – with the possible exception of
86 the ALH 84001 age – may need later revision; the crater chronology of early Mars has not yet been
87 securely calibrated to radiogenic dates (Robbins et al., 2013).

88

89 **2. Details of Small Crater Analysis.**

90 When craters are dispersed through a 3D volume (Edgett & Malin, 2002), the size-frequency
91 distribution of craters exposed at the surface will favor larger craters. This is because a 2D surface

92 cutting through the volume (e.g., the erosion surface) is more likely to intersect a big crater than a
93 small one. This geometric exposure correction is proportional to crater size if craters of different
94 sizes have the same shape. This is approximately true in the strength regime relevant to this paper
95 (Melosh, 1989). If craters of different sizes have the same shape, then crater area is proportional to
96 the square of diameter, but the probability of a plane cutting through a crater is proportional to
97 diameter. Therefore, we apply a correction proportional to crater size.

98

99 In Aeolis Dorsa, sediment moved by small impact events is a small fraction of the total sediment
100 moved by all erosion and sedimentation processes. Therefore, in Aeolis Dorsa, small craters can be
101 thought of as tracer particles with respect to erosion and sedimentation processes. Scale-
102 independence of erosion and sedimentation events (the Sadler effect; Jerolmack & Sadler, 2007;
103 Schumer & Jerolmack, 2009) will tend to preferentially obliterate smaller craters (Ref. 20). This is
104 because smaller craters are more likely to be completely removed with the ‘Cantor dust’ of scale-
105 independent erosion events. This effect is independent of the purely geometric exposure effect
106 discussed in the previous paragraph, although it has the same sign. If the Sadler effect were
107 important for ancient sedimentation on Mars, this would bias our survey towards detecting larger
108 craters. We do not attempt to correct for this bias because we do not know if the Sadler effect was
109 important for ancient sedimentation on Mars. Any correction would lower our paleopressure upper
110 bound, strengthening our conclusions.

111

112 We classified one cluster of craters as ancient (in the SE of DTM 1; Fig. S8a). This may be a
113 primary cluster or alternatively might result from dispersal of secondaries in a thicker atmosphere
114 (Popova et al., 2007). It is possible that future work might use ancient crater clusters to set a lower
115 limit on atmospheric paleopressure.

116

117 We interpret craters mapped as ‘ancient’ that lie between the river deposits as being part of the
118 same (buried/embedded) crater population as craters that are overlain by ancient river deposits. If
119 this interpretation is correct, then a histogram of river-crater interaction frequencies from a Monte
120 Carlo trial should be consistent with the measured proportion of craters overlain by ancient river
121 deposits in the measured ancient-crater population. But if our false positive rate is significantly
122 higher away from the river deposits, this would show up as a reduced proportion of river-crater

123 interactions in the measured ancient-crater population relative to that expected by chance as
124 determined by a Monte Carlo trial. For long, parallel river deposits of spacing W and crater
125 diameter $<$ river-deposit width, the fraction of intersections is approximately D/W . This is
126 consistent with our mapped populations if we make the approximation $W = A/L$ where A is DTM
127 area and L is channel length. However, the geometry of the real river deposits is more complicated
128 than this idealization (Fig. S8). Therefore, to validate our interpretation, we did the following
129 (typical output shown in Fig. S3):-

130

- 131 (1) Mapped the outlines of all channels within the DTMs (Fig. S8);
- 132 (2) Sprinkled random crater populations over the resulting maps, randomly selecting radii from
133 the observed populations and randomizing locations. The number of ‘definite’ craters and
134 the number of rimmed circular mesas is the same as in the mapped distribution. Craters
135 100% obscured by channel deposits were removed with replacement;
- 136 (3) Counted the number of crater-river interactions for this synthetic population (and the areas
137 of overlap);
- 138 (4) Repeated 1,000 times.

139

140 We found that the ‘definite plus Rimmed Circular Mesas’ crater population is in the 56th
141 percentile of the synthetic distribution of crater-river interaction frequencies (Fig. S3). The
142 ‘definite’ crater population has *more* river-crater interactions than 89% of the synthetic
143 populations, which may indicate a higher likelihood that true embedded craters are relegated to
144 ‘candidate’ status away from the river deposits. The Rimmed Circular Mesas have a lower
145 interaction frequency than 90% of the random populations, probably because they are locally high-
146 standing so that horizontally-adjacent river deposits have usually been eroded away. This
147 procedure obviously cannot rule out a small contribution of false positives, but in combination
148 with our geologic checklist (Supplementary Table 1) it validates our interpretation that ancient
149 craters mapped as ‘definite’ between the river deposits do not have a significantly higher false
150 positive rate than ancient craters mapped as ‘definite’ that are overlain by river deposits.

151 **3. Details of data-model comparison.**

152

153 **3a. Additional model details.**

154

155 More details about our forward model of impactor-atmosphere interactions can be found in
156 Williams et al. (2010) and Williams & Pathare (2012). The small-craters technique has been
157 previously applied by Paige et al. (2007) and Kreslavsky (2011) to infer P for relatively recent
158 Martian deposits.

159

160 The size distribution of our synthetic impactor populations follows Brown et al. (2002); the initial-
161 velocity distribution follows Davis (1993). Each population contains 3% irons, 29% chondrites,
162 33% carbonaceous chondrites, 26% cometary objects, and 9% “soft cometary” objects (following
163 Ceplecha et al. 1998) with densities and ablation coefficients k_{ab} also set following Ceplecha et al.
164 1998. Fragmentation occurs when ram pressure $Q_a v^2$ exceeds M_{str} , disruption strength. M_{str} is set to
165 250 kPa; much lower or much higher values would be inconsistent with the observation that more
166 than half of craters observed to form in the current 6 mbar Martian atmosphere are clusters (Daubar
167 et al. 2013). This value of M_{str} is within the range reported for Earth fireballs (Ceplecha et al.
168 1998), and our conclusions are insensitive to M_{str} variations within the Ceplecha et al. (1998)
169 range. We adopt an impactor entry angle distribution that peaks at 45° (Love and Brownlee, 1991).
170 The ratio of the final rim-to-rim diameter to the transient crater diameter is set to 1.3. The
171 excavation efficiency decreases as $1/(v \sin \theta_i)$ where θ_i is the impact angle (Pierazzo & Melosh,
172 2000). We linearly interpolate model output between runs at 0.125, 0.25, 0.5, 1.0, 2.0, 3.0, and 5.0
173 bars to obtain crater size-frequency distributions as a function of P .

174

175 We limit the computational cost of the model by only injecting impactors at the top-of-the-
176 atmosphere that are larger than a cutoff diameter d_c . Holding d_c constant over the wide range of
177 pressures of interest leads to interminably long runs for high atmospheric pressures. This is
178 because building up a smooth cumulative distribution function of predicted crater diameters
179 (colored lines in Fig. 2) requires hundreds of large impactors, but most CPU time is wasted on
180 detailing the fate of numerous small impactors which have a vanishingly small chance of forming
181 high-velocity craters. Therefore, we set increasing cutoff diameters for increasing atmospheric

182 pressure. These $d_c(P)$ were selected for each P ($P > 0.25$ bar) by progressively decreasing the
183 cutoff diameter from a large value until further reductions did not lead to a significant change in
184 model output crater diameter cumulative distribution function.

185

186 **3b. Fitting procedure.**

187

188 Atmospheric pressure was found by bayesian fitting of the data to cratering-model output, treating
189 the impacts as a Poisson process (Aharonson et al., 2003; Ch. 6-7 in Wall & Jenkins, 2012).

190

191 The power-law slope describing the ratio of large to small impactors is fixed, and the crater density
192 is modeled as a function of atmospheric pressure and an overall impactor frequency. Our
193 procedure is analogous to χ -squared fitting, but it is appropriate for the limit where each bin
194 contains a small number of data.

195

196 For each forward model, we ran enough randomized cases to build up a smooth distribution $\lambda =$
197 $p(D, P)$. When fitting the data to the model, the crater diameters are binned in increments of 1 m.

198 For each of these crater-diameter bins, the probability of obtaining the observed number of craters
199 Y in that size bin given was obtained using Poisson statistics:-

200

$$201 \quad p(Y|D, P) = \bar{\lambda}^Y \exp(-\bar{\lambda}) / Y!$$

202

203 where the overbar corresponds to scaling for the overall number of impacts observed. The overall
204 likelihood of the data given the model is the sum of the logs of the probabilities for each crater-
205 diameter bin (e.g. Ch. 6-7 in Wall & Jenkins, 2012; Aharonson et al., 2003). We separately
206 calculated the best fit paleopressure and statistical error using bootstrapping, obtaining similar
207 results (not shown).

208

209 **4. Error analysis and sensitivity tests.**

210 With $\sim 10^2$ craters in our sample, the fractional statistical error in our analysis (Supplementary
211 Section 3b) is $\sim 10\%$. More important are possible systematic errors. In this section, we estimate

212 the individual impact of these possible systematic errors on the conclusions. Because we are
213 reporting an upper limit, we emphasize errors that could raise the upper limit.

214

215 - *False positives and false negatives in identifying ancient craters.* In general, orbital
216 imagery of eroding sedimentary-rock units will show a mix of synerosional (“recent”)
217 craters and syndepositional (ancient/embedded) craters. Only the ancient craters constrain
218 ancient atmospheric pressure. Because the modern atmosphere of Mars is thin and permits
219 numerous small craters to form, many small craters counted as ancient will be false
220 positives *unless* the base rate of embedded craters is high, or unless the procedure for
221 identifying embedded craters is very accurate (Supplementary Table 1). At the stratigraphic
222 levels mapped in this paper, we observe many craters incompletely overlain by river
223 deposits. Because most of the surface area is not close to the edge of a river deposit (Fig.
224 S8), craters formed in most places would not be overlain by river deposits, or would be
225 completely masked by river deposits (Fig. S8). The observation that many craters are
226 incompletely overlain by river deposits indicates that the base rate of embedded craters is
227 high. Because cratering is random, we expect many embedded craters away from river
228 deposits, and this is consistent with our Monte Carlo results (Supplementary Section 2).

229

230 False negatives could in principle bias the results to higher or lower pressures. We
231 documented all “candidate” ancient craters and found that they are smaller on average than
232 the craters used to construct our paleopressure fit (as might be expected from resolution
233 effects). Therefore false negatives do not affect the validity of our upper limit. Having
234 shown that the candidate population does not affect our upper limit, we now provide an
235 extended discussion of this crater population. The ‘candidate’ exhumed craters – which by
236 definition are not definitely exhumed - may be significantly contaminated by synerosional
237 craters. The regional $N(1)$ count is consistent with a landscape that is currently being
238 sanded down at $\sim 1 \mu\text{m}/\text{yr}$. Assuming steady state resurfacing with equilibrium between
239 production and obliteration, and ignoring aeolian bedforms, this erosion rate could permit a
240 considerable number of degraded synerosional craters to form in the modern thin
241 atmosphere. However, we do not see many pristine (rayed, blocky, or deep) $D \sim 50\text{m}$
242 craters. It is possible that the balance is made up by ‘candidate’ exhumed craters that are in

243 fact relatively recent synerosional craters which have lost their rims. The potential for rapid
244 degradation of crater rims in the modern Mars environment is supported qualitatively by
245 evidence of rapid degradation of small craters formed in sedimentary rocks along the
246 Opportunity traverse (Golombek et al., 2010) and rapid degradation of boulders on young
247 fans (Haas et al., 2013). If we are wrong and the candidate exhumed craters are all
248 syndepositional, then our paleopressure upper bound would be lowered by a factor of ~ 2 ,
249 strengthening our conclusions.

250

251 Channels and channel deposits are identified on the basis of network/tributary structure
252 (Fig. S8), preserved sedimentary structures such as point bars, and double-ridge shape
253 (Williams et al. 2013) in DTM cross-sections. In Aeolis Dorsa, channels are easily
254 distinguished from postdepositional features such as faults.

255

256 - *Top-of-atmosphere parameters.* Our model uses a modern (Near Earth Object-like) size-
257 frequency distribution of impactors (Brown et al., 2002), which is relatively rich in small
258 impactors due to faster drift of small asteroids into destabilizing orbital resonances with
259 Jupiter (Strom et al., 2005). This is appropriate for stratigraphic units postdating the Late
260 Heavy Bombardment (see discussion of “Age Control” above); the large rivers on Mars
261 that have been mapped so far were last active significantly after the Late Heavy
262 Bombardment (Fassett & Head, 2008; Hoke & Hynek 2009). If we are wrong and the
263 rivers date from the time of the Late Heavy Bombardment, then the small-impactor-poor
264 impactor size-frequency distribution inferred for the Late Heavy Bombardment by Strom et
265 al. (2005) may be appropriate. In that case, the observation of a large proportion of small
266 impact craters requires an even lower P than reported here, and our paleopressure
267 conclusions are strengthened.

268

269 - *Impact parameters and postdepositional modification of impact size and shape.* Crater
270 volume scalings are a physically-motivated fit to experimental data (Holsapple, 1993).
271 Predicted volumes are only accurate to a factor of ~ 2 . Among the parameters in the π -group
272 scaling, the most important parameter sensitivity of the model is to target strength. The
273 strongest rock targets produce decrease in crater size of up to a factor of 2, and a

274 comparable increase in the paleopressure upper bound (Fig. S4b), relative to our preferred
275 rock-mass strength of 65 kPa (Refs. 21, 22; see also
276 <http://keith.aa.washington.edu/craterdata/scaling/theory.pdf>). Our main argument against
277 adopting strong-rock rock-mass-strength for our model is geological – because of the
278 observed fine layering and high density of river deposits (Refs. 11, 20; Fig. S1), the
279 simplest interpretation of geological units “F1” and “F2” is that they are fluvial/alluvial or
280 other weak sedimentary deposits, analogous to terrestrial desert alluvium. Desert alluvium
281 has been thoroughly characterized through Nevada Test Site explosions of comparable
282 energy to the small natural high-velocity impact craters used in this paper, and an empirical
283 rock-mass strength of ~65 kPa is inferred. This is the value that we use in this paper.
284 Crucially, the *present-day* outcrop strength of the Aeolis Dorsa deposits is irrelevant,
285 because embedded craters formed early in the history of the deposits and the timing of any
286 compaction or cementation is unknown. Model output is not very sensitive to the details of
287 how fragmentation is parameterized ($\lesssim 10\%$; Fig. S4a), nor to target density ($\lesssim 25\%$ for
288 range 1500-2500 kg/m³; Fig. S4c), nor to reasonable variations in the mix of impactor
289 strengths and densities (e.g., the stone:iron ratio; not shown). Setting $\mu = 0.55$ (as opposed
290 to our adopted value of $\mu = 0.41$; Methods) is reasonable if ice, groundwater, or diagenetic
291 cements filled the pore spaces of the target material. For fixed target strength, this increases
292 crater diameters, typically by a factor of $\sim 5/3$ (Fig. S4b). If $\mu = 0.55$ then (holding all
293 other parameters constant) the observed small impact craters would correspond to even
294 smaller impactors surviving passage through the paleoatmosphere. This would strengthen
295 our conclusions.

296

297 - As discussed in the main text, *erosion may modify craters*. Our main safeguard against this
298 source of error is to fit the circles defining the crater diameters only to parts of the crater
299 edge which are well-preserved. A supplementary safeguard is to expand (or contract) the
300 resulting circles until they enclose only two (or enclose all *except* two) of the hand-picked
301 points on the crater rim. We then define the annulus enclosed by these minimal and
302 maximal circles as a ‘preservation-error annulus.’ This accounts for possible erosional
303 modification of crater shapes, assumed to be initially close to circular (Melosh, 1989). The
304 full width of the annulus was $(13\pm 6)\%$ of nominal diameter for definite embedded craters

305 and $(16\pm 7)\%$ of nominal diameter for RCMs. We found no significant difference between
306 total errors (from resampling) including random sampling of radii from within the
307 preservation-error annulus as opposed to total resampling errors excluding this effect.

308

309 - *Errors in elevation* propagate to errors in the final Mars paleo-atmospheric pressure
310 estimate because they affect the hydrostatic correction of pressure to zero elevation (i.e. to
311 the Mars datum). In this context, the intrinsic error of the DTMs is negligible ($\ll 100$ m),
312 because they are controlled to the Mars Orbiter Laser Altimeter dataset which has a radial
313 precision of ~ 1 m (Smith et al., 2001). The elevation range of the studied craters is ~ 0.1 km
314 ($\sim 1\%$ of an atmospheric scale height), which is also negligible. Even if postdepositional
315 tectonic uplift/subsidence of the studied terrain had an amplitude of 1 km (which is
316 unlikely), this would introduce a systematic error of only $\sim 10\%$.

317

318 In summary, the error in our upper limit on P is set primarily by uncertainty in the effective rock-
319 mass strength of the target at the time of impact. Our chosen strength value follows from our
320 geologic interpretation of the target materials; if our geologic interpretation is correct, then the P
321 error due to strength uncertainty is $< 50\%$. If our geologic interpretation is incorrect, then this could
322 introduce an error of (at most) a factor of 2, but this is counterbalanced to some degree by the
323 possibility that μ was higher than the value we have chosen here. In the future, small-scale lab
324 experiments, crater-counts of geologic materials of similar age but different strengths (e.g. Ref.
325 21), and ground-truth from rover observations could better constrain these errors.

326

327 **5. DTM extraction procedure.**

328 The procedure used for DTM extraction follows that of Ref. 10 and uses the NGATE algorithm
329 (Zhang, 2006) and SOCET SET software. The HiRISE images making up the
330 PSP_007474_1745/ESP_024497_1745 steropair have emission angles of 4.5° and 30°
331 respectively, and map scales of 25 cm/pixel and 50 cm/pixel respectively. The coarser image
332 (ESP_024497_1745 in this case) determines the optimal spatial resolution for the topographic
333 extraction, so we derived a 2.5 m/post DTM for this pair (DTM1). MOLA PEDRs were used as
334 ground control points, with vertical accuracy set to 10 m, as the area contains mostly flat smooth
335 features, for which it is difficult to link PEDR shots to surface features observed at HiRISE scale.

336 In addition, we generated our own gridded MOLA DTM (from PEDR), which we used as a seed
337 for extraction. The process for DTM2 was very similar (emission angles 2° and 18°; map scales of
338 50 cm/pixel for both images).

339

340 We used several metrics for DTM validation and quality assessment. These included LE90 (Linear
341 Error of 90%). This value is automatically computed (by the SOCET SET photogrammetry
342 software) as the error in elevation of one point with respect to another point within the DTM at
343 90% probability. In DTM1, the mean LE90 is 1.07 m and when correlation had succeeded, the
344 highest value is 3 m. These values should be compared with the theoretical limit
345 on vertical precision using the standard photogrammetry equation (Ref. 10):

346

347

$$EP = r s / (b/h)$$

348

349 where EP is the expected vertical precision, r is the accuracy with which features can be matched
350 (i.e., $r = 0.3$), s the ground sample distance (i.e., $s = 50$ cm), and the b/h ratio describes the
351 convergence geometry of the stereopair (i.e., $b/h \sim 0.5$). These values give $EP \sim 0.3$ m. As a test,
352 the shaded relief was compared to the orthophoto using the same illumination geometry over a
353 constant albedo area (Figs. S5, S6). We also compared cross-sections over both the HiRISE image
354 and the shaded relief computed from the DTM. A good match was obtained.

355

356 **Supplementary References.**

357 Aharonson, O., Schorghofer, N., & Gerstell, M.F., Slope streak formation and dust deposition rates on
358 Mars, *J. Geophys. Res.* **108**, 5138 (2003).

359 Brown P., Spalding, R. E., ReVelle, D.O., Tagliaferri, E. & S. P. Worden, The flux of small near-Earth
360 objects colliding with the Earth, *Nature* **420**, 294–296 (2002).

361 Ceplecha, Z., et al., Meteor phenomena and bodies, *Space Sci. Rev.* **84**, 327-341 (1998).

362 Daubar, I.J., et al., The current martian cratering rate, *Icarus* **225**, 506-516 (2013).

363 Davis, P., Meteoroid impacts as seismic sources on Mars, *Icarus* **105**, 469-478 (1993).

364 Edgett, K.S. & Malin, M.C., Martian sedimentary rock stratigraphy: Outcrops and interbedded craters of
365 northwest Sinus Meridiani and southwest Arabia Terra, *Geophys. Res. Lett.* **29**, CiteID 2179 (2002).

366 Ehlmann, B.L., et al., Evidence for low-grade metamorphism, hydrothermal alteration, and diagenesis
367 on Mars from phyllosilicate mineral assemblages, *Clays and Clay Minerals* **59**, 359-377 (2011).

368 Fassett, C.I., & Head, J.W., The timing of martian valley network activity: Constraints from buffered crater
369 counting. *Icarus* **195**, 61–89 (2008).

370 Fassett, C.I., & Head, J.W., Sequence and timing of conditions on early Mars. *Icarus* **211**, 1204-1214
371 (2011).

372 Golombek, M., et al., Constraints on ripple migration at Meridiani Planum from Opportunity and HiRISE
373 observations of fresh craters: *J. Geophys. Res.* **115**, E00F08 (2010).

374 Greeley, R., et al., Fluid lava flows in Gusev crater, Mars, *J. Geophys. Res.*, **110**, E05008 (2005).

375 Haas, T., Hauber, E., & Kleinhaus, M.G., Local late Amazonian boulder breakdown and denudation rate on
376 Mars, *Geophys. Res. Lett.*, **40**, 3527-3531 (2013).

377 Hartmann, W.K. & Neukum, G., Cratering Chronology and the Evolution of Mars, *Space Sci. Rev.* **96**, 165-
378 194 (2001).

379 Hoke, M.R.T., & Hynek, B.M., Roaming zones of precipitation on ancient Mars as recorded in valley
380 networks, *J. Geophys. Res.* **114**, E08002 (2009).

381 Howard, A.D., Moore, J.M., & Irwin, R.P., An intense terminal epoch of widespread fluvial activity on
382 early Mars: 1. Valley network incision and associated deposits, *J. Geophys. Res.* **110**, E12S14 (2005).

383 Irwin, R.P., & Watters, T.R., Geology of the Martian crustal dichotomy boundary: Age, modifications, and
384 implications for modeling efforts, *J. Geophys. Res.* **115**, E11006 (2010).

385 Jerolmack, D.J. & Sadler, P., Transience and persistence in the depositional record of continental margins.
386 *J. Geophys. Res.* **112**, F03S13 (2007).

387 Kreslavsky, M. A., Observational constraints on atmospheric pressure on Mars in the Amazonian, *Fourth*
388 *International Workshop on the Mars Atmosphere: Modelling and observation*, Paris, France (2011).

389 Le Deit, L., et al., Sequence of infilling events in Gale Crater, Mars: Results from morphology, stratigraphy,
390 and mineralogy, *J. Geophys. Res.* **118**, 2439-2473 (2013).

391 Lefort, A., Burr, D.M., Beyer, R.A., and Howard, A.D, Inverted fluvial features in the Aeolis-Zephyria
392 Plana, western Medusae Fossae Formation, Mars: Evidence for post-formation modification, *J. Geophys.*
393 *Res.* **117**, E03007 (2012).

394 Love, S.G. & Brownlee D.E., Heating and thermal transformation of micrometeoroids entering the Earth's
395 atmosphere, *Icarus* **89**, 26-43 (1991).

396 Melosh, H.J., *Impact cratering: A geologic process*, Oxford University Press, Oxford, UK (1989).

397 Michael G.G., & Neukum G., Planetary surface dating from crater size-frequency distribution
398 measurements: Partial resurfacing events and statistical age uncertainty, *Earth & Planet. Sci. Lett.*, **294**, 223-
399 229 (2010).

400 Paige, D.A., et al., MER small crater statistics: Evidence against recent quasi-periodic climate variations, in
401 *7th Intl. Conf. on Mars*, 3392 (2007).

402 Pierazzo, E., & H.J. Melosh, Understanding oblique impacts from experiments, observations, and modeling,
403 *Annu. Rev. Earth Planet. Sci.* **28**, 141-168 (2000).

404 Popova, O.P., et al., Crater clusters on Mars: Shedding light on martian ejecta launch conditions, *Icarus*
405 **190**, 50-73 (2007).

406 Robbins, S.J., Hynek, B.M., Lillis, R.J., & Bottke, W.F., Large impact crater histories of Mars: the effect of
407 different model crater age techniques, *Icarus* **225**, 173–184 (2013).

408 Schumer, R., & Jerolmack, J.D., Real and apparent changes in sediment deposition rates through time, *J.*
409 *Geophys. Res.* **114**, F00A06 (2009).

410 Smith, D.E., et al., Mars Orbiter Laser Altimeter: Experiment summary after the first year of global
411 mapping of Mars, *J. Geophys. Res.* **106**, 23869-23722 (2001).

412 Smith, M.R., Gillespie, A.R., and Montgomery, D.R., Effect of obliteration on crater-count chronologies for
413 Martian surfaces, *Geophys. Res. Lett.* **35**, L1202 (2008).

414 Stanley, B.D., Hirschmann, M.M., & Withers, A.C., CO₂ solubility in Martian basalts and Martian
415 atmospheric evolution, *Geochimica et Cosmochimica Acta* **75**, 5987-6003 (2011).

416 Strom, R.G., et al., The Origin of Planetary Impactors in the Inner Solar System, *Science* **309**, 1847 (2005).

417 Wall, J.V. & Jenkins, C.R., Practical statistics for astronomers, 2nd Edition (Cambridge Observing
418 Handbooks for Research Astronomers), Cambridge University Press, Cambridge, UK (2012).

419 Werner, S.C. & Tanaka, K.L., Redefinition of the crater-density and absolute-age boundaries for the
420 chronostratigraphic system of Mars, *Icarus* **215**, 603-607 (2011).

421 Williams, J.-P., Aharonson, O., & Pathare, A.V., The production of small primary craters on Mars, in 41st
422 *Lunar Planet. Sci. Conf.*, abstract no. 2574 (2010).

423 Williams, J.-P., & Pathare, A.V., Scaling effective diameters of small impact crater clusters on Mars, in 43rd
424 *Lunar Planet. Sci. Conf.*, abstract no. 2881 (2012).

425 Williams, R.M.E., et al., Variability in martian sinuous ridge form: Case study of Aeolis Serpens in the
426 Aeolis Dorsa, Mars, and insight from the Mirackina paleoriver, South Australia, *Icarus* **225**, 308-324
427 (2013).

428 Zhang, B., Towards a higher level of automation in softcopy photogrammetry: NGATE and LIDAR
429 processing in SOCET SET®, paper presented at GeoCue Corporation 2nd Annual Technical Exchange
430 Conference, Nashville, Tenn. (2006).

431 Zimbelman, J.R., & Scheidt, S.P., Hesperian age for Western Medusae Fossae Formation, Mars, *Science*
432 **336**, 1683 (2012).

433 **Supplementary Table 1: Checklist for identifying ancient craters.**
434 Figure S7 shows examples of applying the checklist, and Figure S8 shows the crater maps
435 resulting from applying the checklist.
436
437

Checklist for accepting ancient craters

Must be an impact structure that is embedded within the stratigraphy.

- Crater, or crater rim (if preserved), or ejecta (if preserved) are crosscut by fluvial deposits → accept
- Crater, or crater rim (if preserved), or ejecta (if preserved) are crosscut by fluvial channels → accept
- Crater partly overlain by sediments topographically, stratigraphically or texturally continuous with surrounding layered sediments → accept
- Crater forms a rimmed circular mesa
- Crater forms a rimmed circular mesa with flat or inward-dipping strata inside the rim; these strata need not be continuous with sediment outside (and usually are not)

Other checks:

- At same or similar level and spatially adjacent to an ancient crater; has the same preservation style (e.g., layered circular mesa) as that ancient crater
- Crater is close to circular (ellipticity < 1.15)

- Rim or edge preserved topographically in DTM over at least 180° of arc (does not have to be continuous)

or

- Crater appears to be concave-up in anaglyph

if neither:

- Reject.

Ensemble checks:

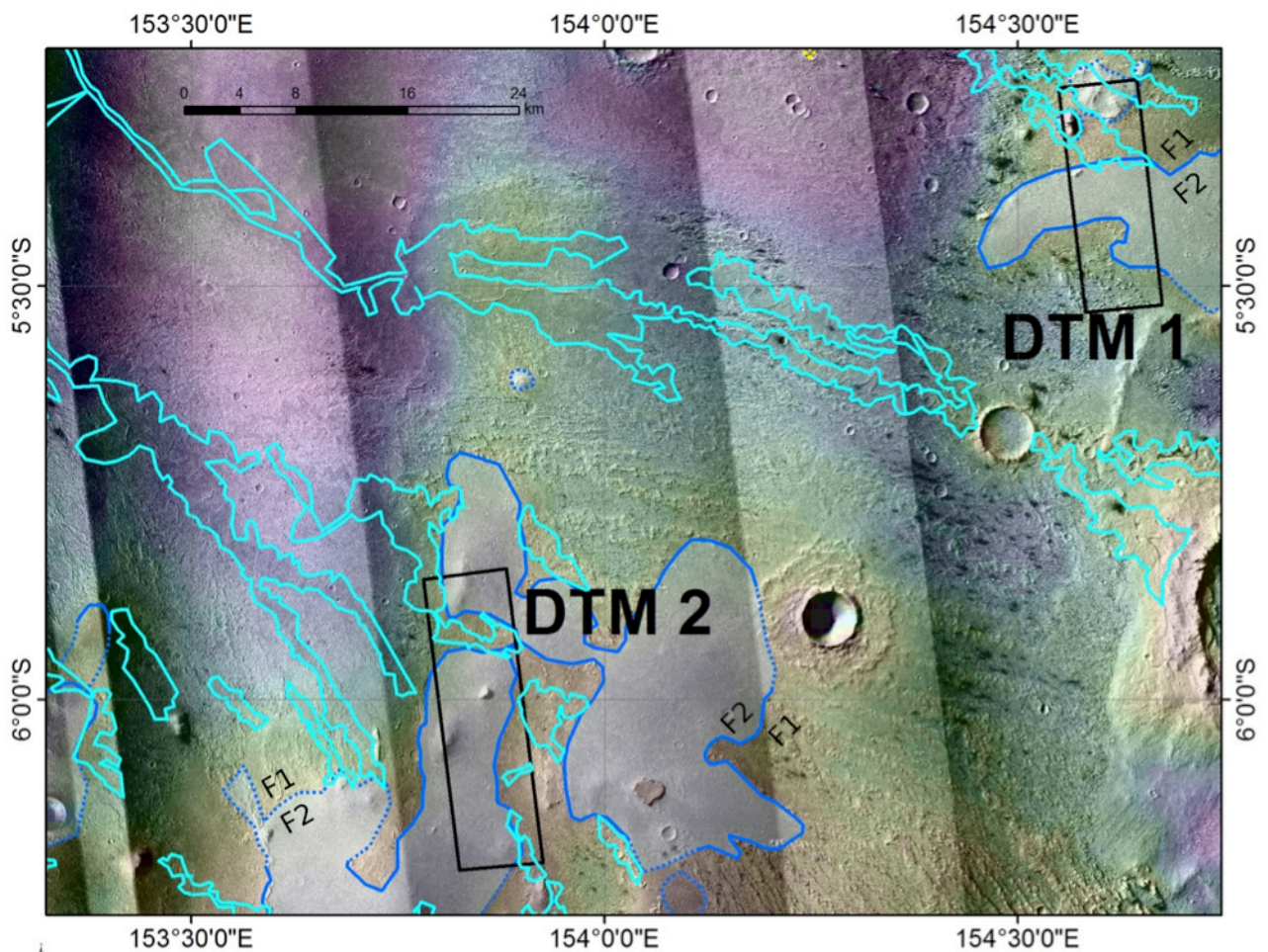
- Is the same preservation style of craters found beyond the mapped background geologic unit in this geologic region? (If so, could be a younger mantling unit: reject all craters)
- Are the ellipticities aligned?
- Is the distribution of crater centers random in space?
- Are any clusters of craters restricted to a particular stratigraphic level or a particular geologic unit? (If so, suspect soft-sediment deformation).

Checklist for rejecting ancient craters: rejects override accepts***Either not clearly an impact structure, or not embedded within stratigraphy***

- Rim preserved mostly (>2/3) intact, and rim ellipticity > 1.5 → immediate reject
- Crater (and ejecta, if visible) are not superposed by anything other than active/recently active bedforms → immediate reject
- Rays visible → immediate reject
- Crater could be a prolongation of nearby soft-sediment deformation texture consisting of cells with upcurled edges ('spatulate' soft-sediment deformation).
- (For circular mesas) The height of the mesa exceeds the radius of the flat top or rim by >1.5 (risk of being a rootless cone or explosion pit analogous to von Braun/Goddard at the Spirit field site in Gusev crater).
- There is a rim visible around all or most of the top of the structure, but the elevation of the rim is much lower on one side of the structure (immediate reject; suggestive of volcanism or soft-sediment deformation)

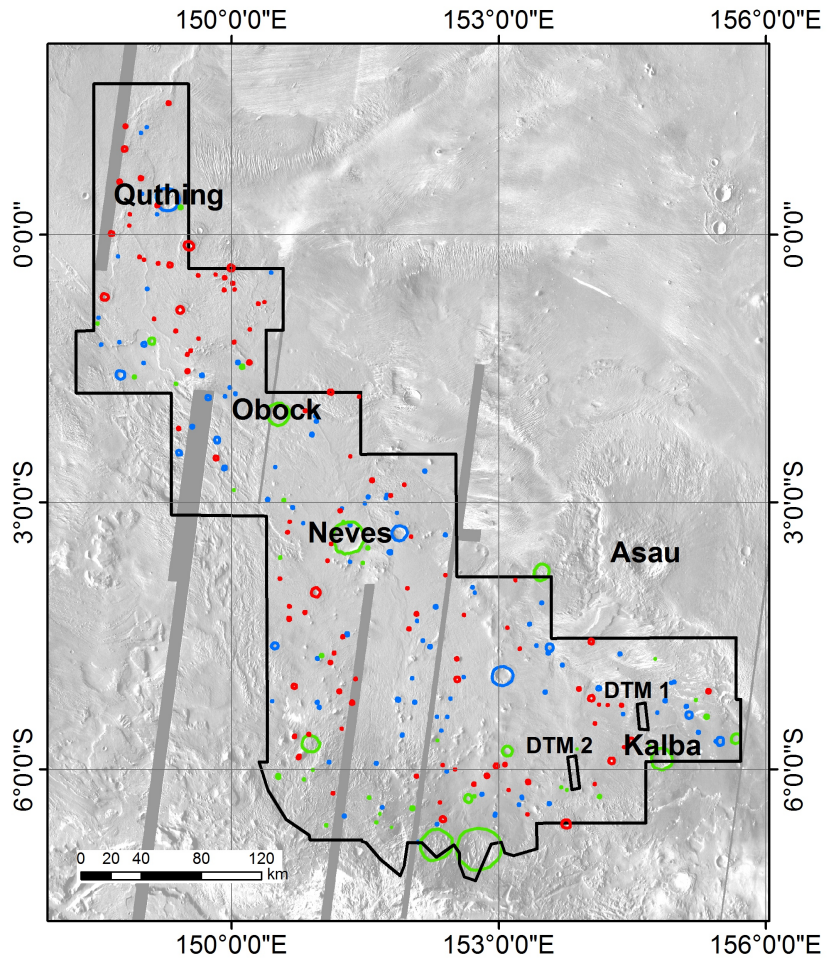
Ensemble level checks for circular mesas - Is there a connection between the relief of the mesa and the diameter of the depression on top? if yes, argues for explosive cone rather than eroded/exhumed impact crater.

438 **Supplementary Figures.**
439



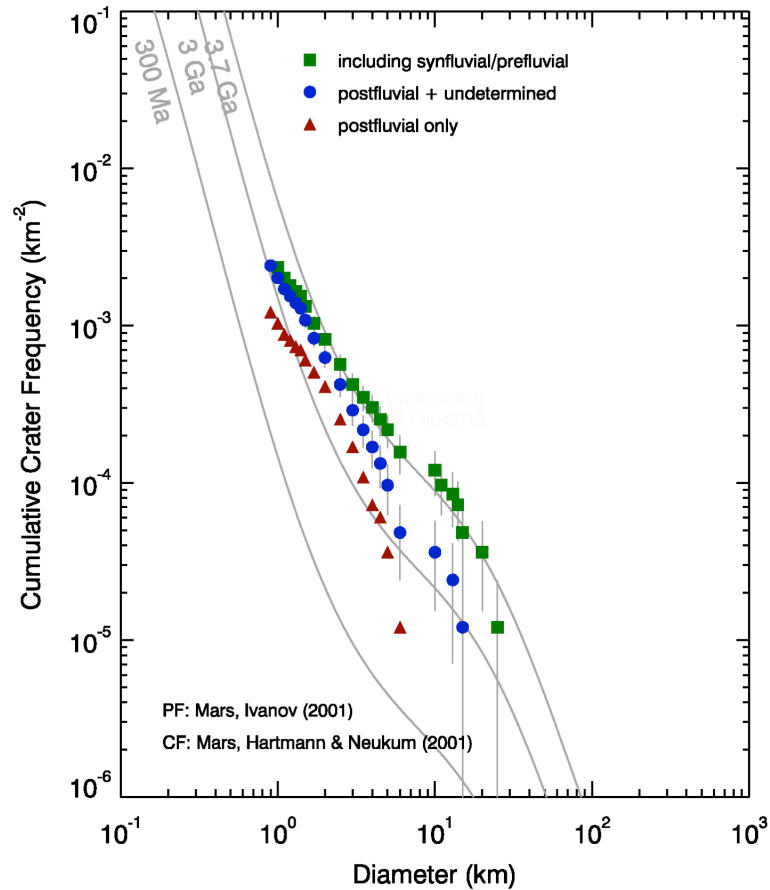
440
441 **Figure S1.** Geologic context for this study. Topographically lower fluvial unit (“F1”, no tint)
442 contains large meander belts (cyan outlines). Topographically higher fluvial unit (“F2”, white tint)
443 contains many river deposits but lacks large meander belts. F1/F2 contact is shown as a solid blue
444 line where mapped with high confidence, and as a dotted blue line where inferred. Background
445 color is cued to MOLA topography (elevation range ~ 500m). Background image is CTX mosaic;
446 the western rim of Kalba crater is visible at right. DTMs were constructed from HiRISE images
447 PSP_007474_1745/ESP_024497_1745 (DTM 1) and ESP_017548_1740/ESP_019104_1740
448 (DTM 2). DTM1 area is 108 km²; DTM2 area is 86 km². See Fig. S8 for details of DTMs.
449

450



451
452

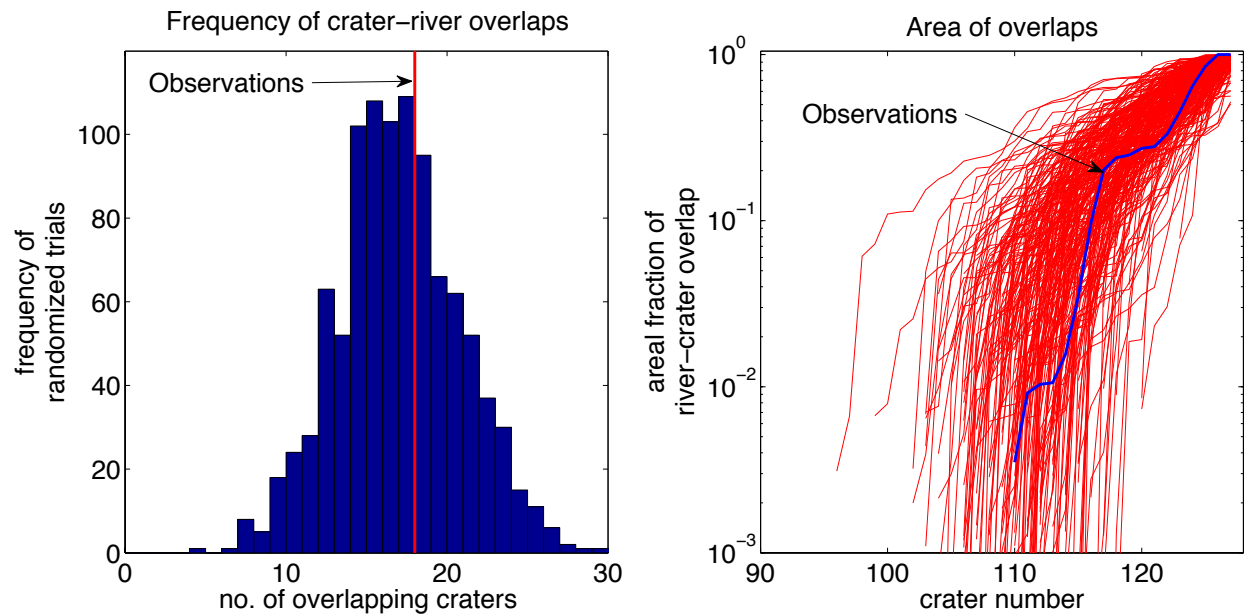
a)



453
 454
 455
 456
 457
 458
 459
 460
 461
 462
 463
 464
 465
 466
 467

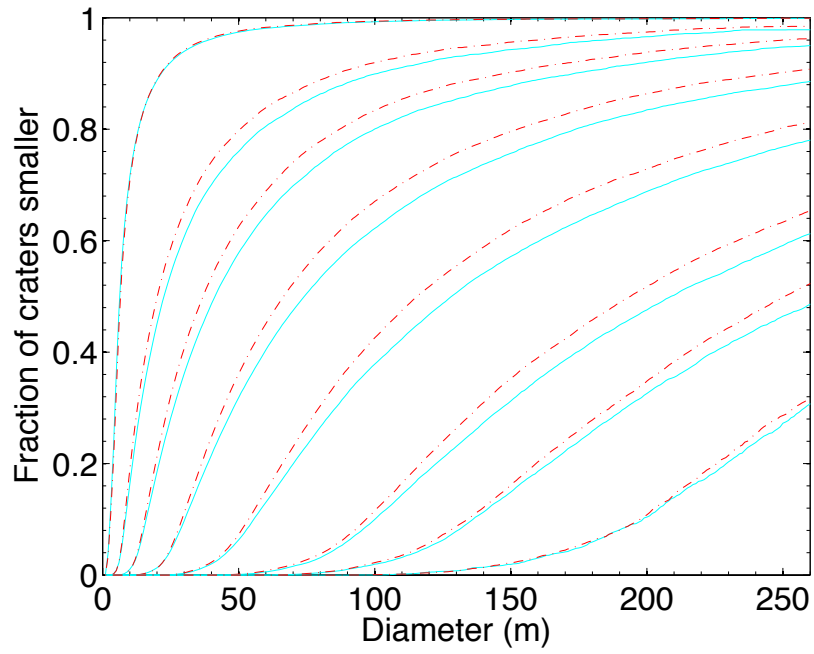
b)

Figure S2. Chronologic context for this study. a) Locations of all craters >1km diameter. Red corresponds to craters that are postfluvial based on local crosscutting relationships; blue corresponds to craters with an undetermined crosscutting relationship to nearby rivers (these are interpreted to be mostly postfluvial on the basis of crater morphology); and green corresponds to synfluvial/prefluvial craters. Black polygon corresponds to perimeter of count area ($8.3 \times 10^4 \text{ km}^2$). Background is THEMIS VIS mosaic. b) Cumulative crater size-frequency distributions plotted using craterstats2 (Michael & Neukum 2010). Error bars show 1σ statistical error. Red: postfluvial craters only. Nominal age considering only crater diameters >2 km is 3.44 (+0.06/-0.10) Ga. Blue: additionally including “undetermined” craters. Nominal age considering only crater diameters >2 km is 3.61 (+0.03/-0.04) Ga. We consider this a lower bound on the true age of Aeolis Dorsa rivers (see text). Green: additionally including prefluvial/synfluvial craters. Nominal age considering only crater diameters >2 km is 3.71 (+0.02/-0.03) Ga.



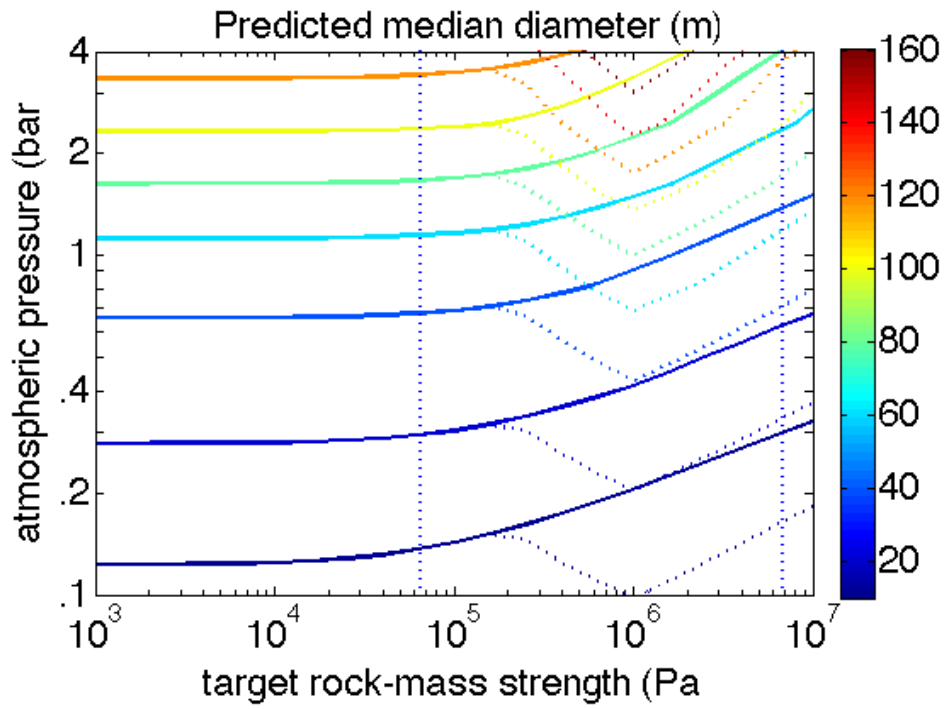
469

470 **Figure S3.** Comparison of crater-river interactions in the observed population to an ensemble of
 471 synthetic crater populations with the same size-frequency distribution. For assumptions, see text.
 472 Left panel: Frequency of crater-river overlaps for 1,000 synthetic crater populations (observations
 473 shown by vertical red line). Right panel: Crosscut test comparing observed crater-river interaction
 474 areas to an ensemble of 1,000 synthetic crater-populations. Ordinate corresponds to fractional area
 475 of overlap for each crater – for legibility, only every fourth synthetic population is shown. Craters
 476 are sorted by fractional overlap – the majority of craters in the synthetic and observed populations
 477 have zero overlap. Observations are shown by thick blue line.



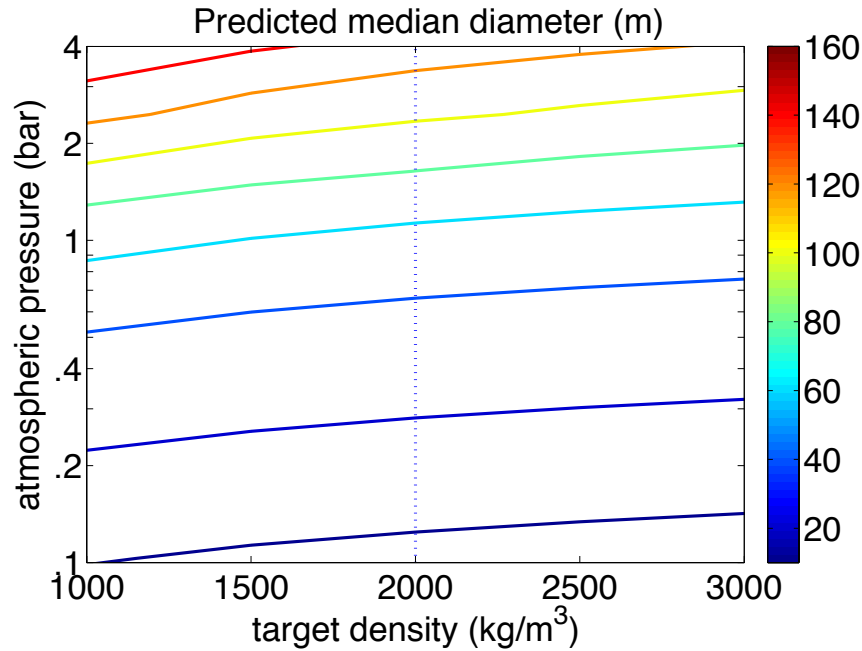
478

(a)



479

(b)

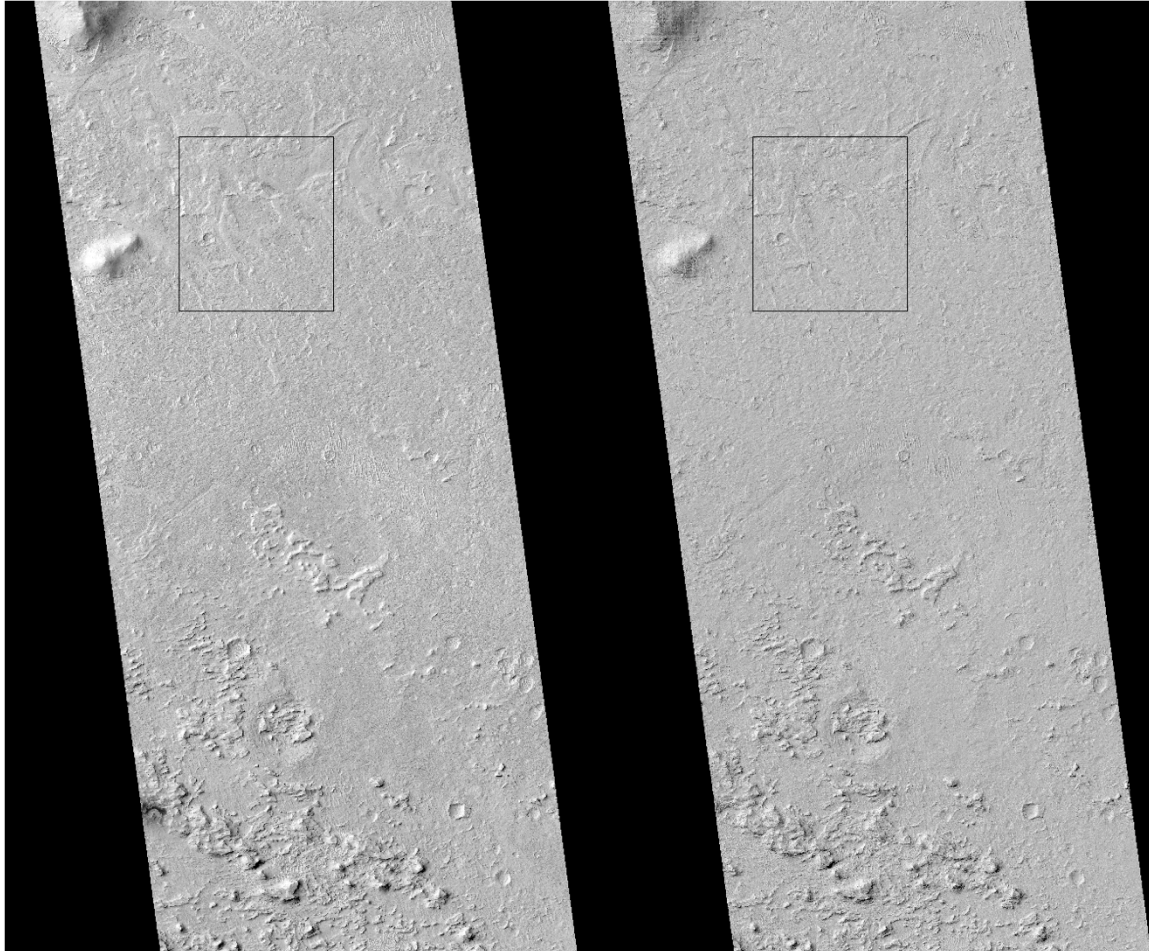


480

(c)

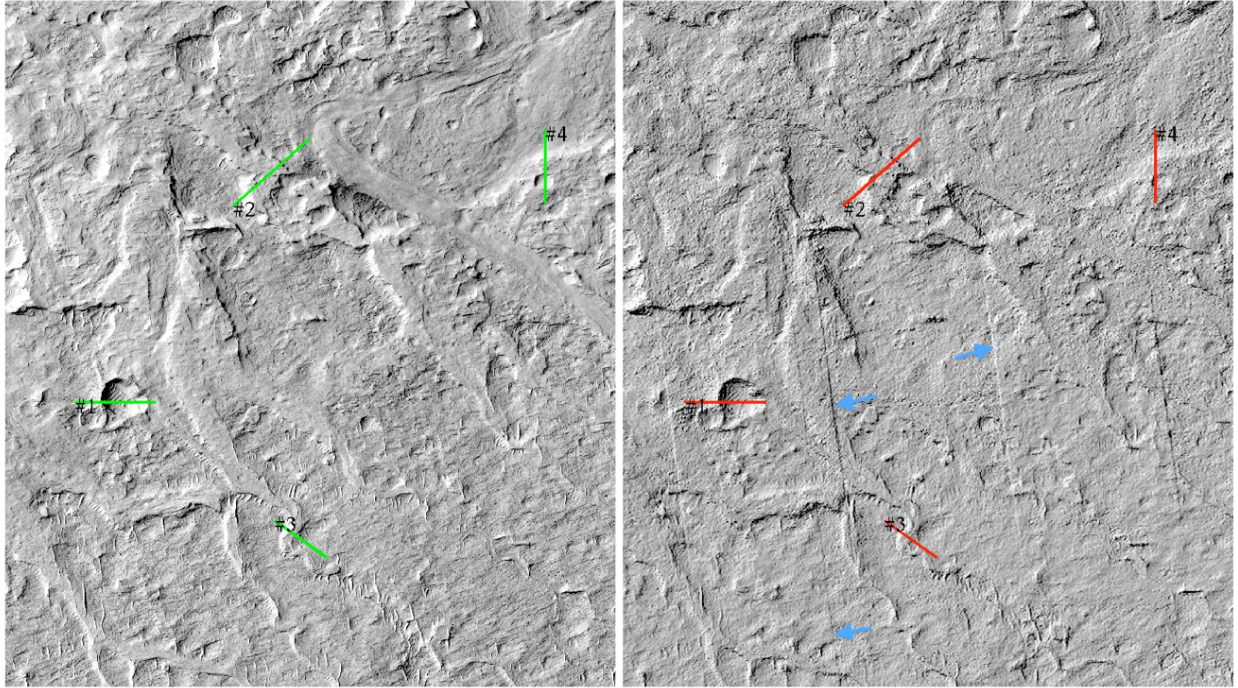
481

482 **Figure S4.** Sensitivity tests. (a) Fragmentation parameterization: cyan solid lines show crater sizes
 483 ignoring the last fragmentation event; red dashed lines show “effective” size of impact combining
 484 all fragments into one “effective” cluster. From left to right, pressures are for 6 mbar, 125 mbar,
 485 250 mbar, 500 mbar, 1 bar, 2 bar, 3 bar and 5bar (assuming impacts at 0m elevation). (b)
 486 Sensitivity to target rock-mass strength (using π -group scaling; Refs. 14, 22). Contours drawn at
 487 median crater size of 10 m, 20 m, 40 m, and then at 20 m intervals until 160 m. Left vertical
 488 dashed line (65 kPa) is strength inferred for desert alluvium (Ref. 14), which is appropriate to our
 489 geologic setting. Right vertical dashed line (6.9 MPa) is “hard rocks” value used by Ref. 22 (their
 490 Figure 7). Solid lines correspond to constant $\mu = 0.41$; colored dashed lines show effect of log-
 491 linear ramp of μ from 0.41 at 200 kPa to 0.55 at 1 MPa and constant thereafter
 492 (<http://keith.aa.washington.edu/craterdata/scaling/theory.pdf>). If the
 493 Aeolis Dorsa sediments had “hard rock”-like strength and $\mu = 0.41$ at the time the craters formed,
 494 then our upper limit is significantly relaxed. (c) Sensitivity to target density (using π -group
 495 scaling): Contours drawn at median crater size of 10 m, 20 m, 40 m, and then at 20 m intervals
 496 until 140 m. Vertical dashed line is our preferred value (2000 kg/m³); a reasonable range is 1500 –
 497 2500 kg/m³, for which inferred-paleopressure variations are modest.



498

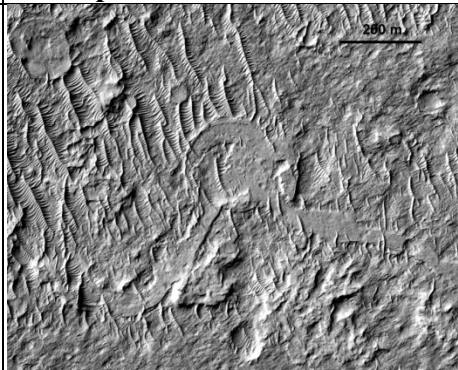
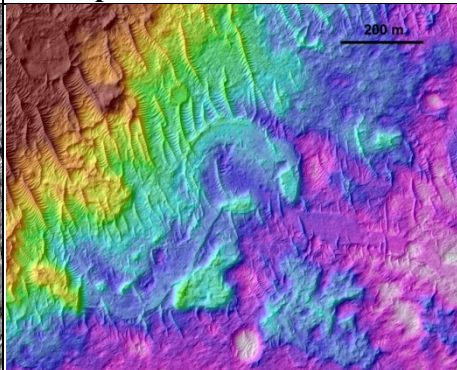
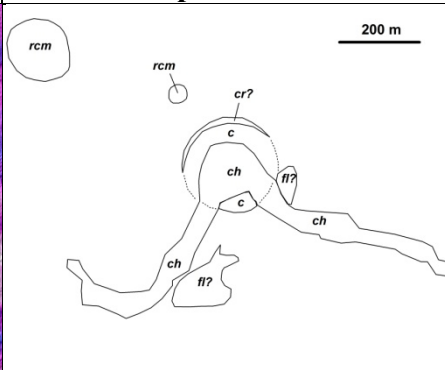
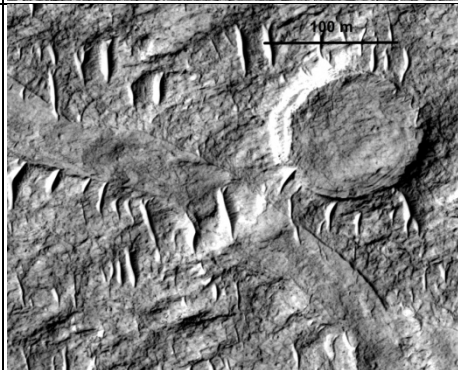
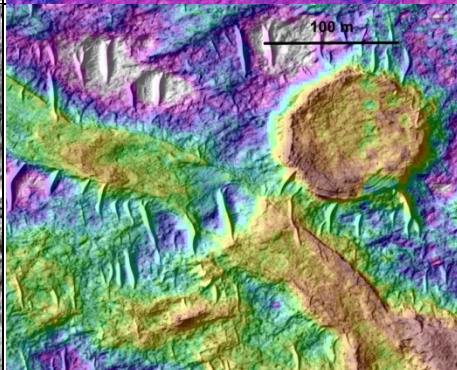
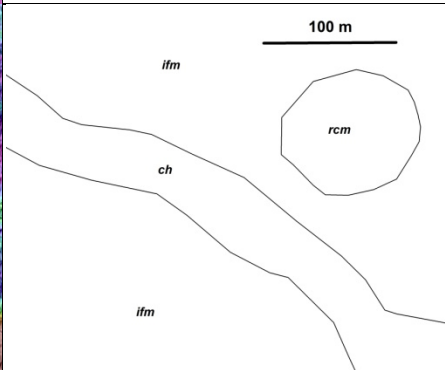

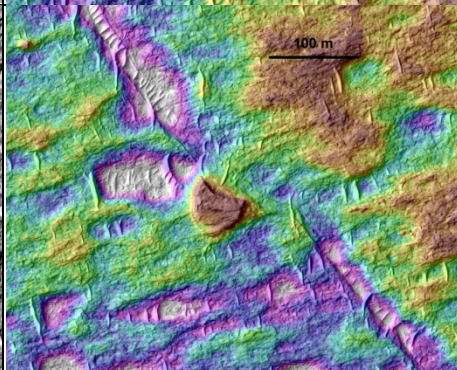
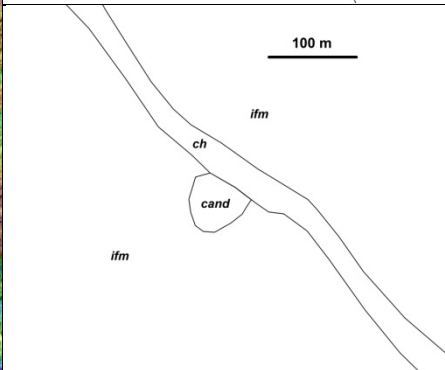
499 **Figure S5.** PSP_007474_1745 image on left, shaded relief of corresponding DTM (DTM1,
500 PSP_007474_1745/ESP_024497_1745) on right illuminated using the same illumination geometry
501 as the image. Black box shows region highlighted in Fig. S6.



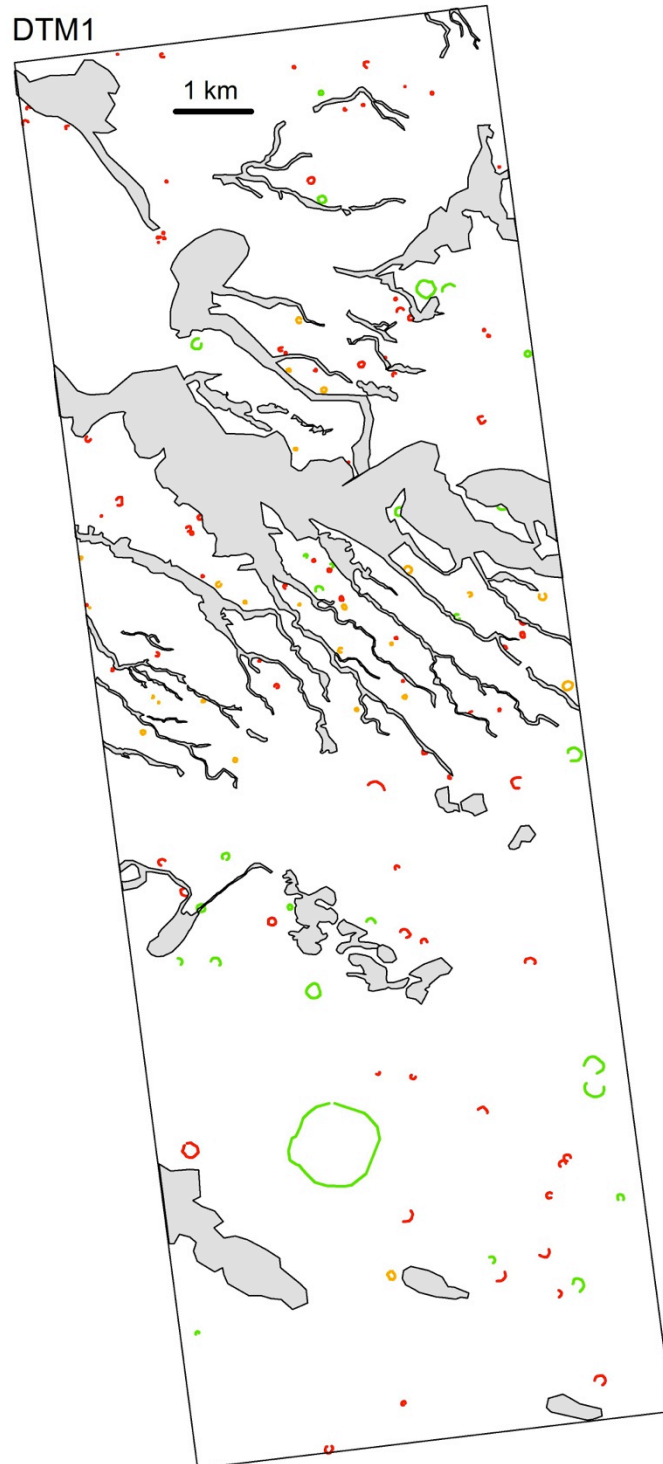
502

503 **Figure S6.** Comparison between HiRISE image and a shaded relief of the corresponding stereo
504 DTM using the same illumination geometry. Left panel: PSP_007474_1745 image (25cm/pixel).
505 Right panel: shaded relief from the stereo extraction. Seams at the boundaries between HiRISE
506 CCDs are visible in the DTM (blue arrows on right panel). Their obvious presence makes it
507 possible to take them into account in any measurement. Red and green profiles highlight points of
508 agreement.

509 **Figure S7.** Examples of application of the checklist in Supplementary Table 1 (anaglyphs not shown). DEF = definite embedded crater;
 510 RCM = rimmed circular mesa; CAND = candidate ancient crater (excluded from paleopressure calculations). Key to sketch interpretations:
 511 *c* – crater or crater fill; *cand* – candidate ancient crater; *ch* – channel or channel-fill material; *cr* – crater rim material; *fl* – fluvial deposits
 512 not part of an integrated channel; *ifm* –interfluve material (unknown origin; simplest interpretation is fluvial overbank material); *rcm* –
 513 rimmed circular mesa.

Type	Orthophoto	Orthophoto + DTM	Sketch interpretation	Notes
DEF				Crater is crosscut by fluvial deposits that are topographically and texturally continuous with those outside crater. Crater is close to circular. Rim or edge is preserved (discontinuously) over more than 180° of arc. → DEF. ESP_017548_1740. See also Figure 1 for additional examples of definite embedded craters. This crater is entry #8 from the Supplementary Table of Ref. 20.
RCM				Crater forms a rimmed mesa. Ellipticity is < 1.15. Rim is preserved (based on DTM and image shading) over more than 180° of arc. Crater appears concave-up in anaglyph and in DTM. No evidence for rays, ejecta, or nearby soft-sediment deformation of similar style. Elevation of mesa ~4m, much less than mesa diameter. → RCM. PSP_07474_1745.
CAND				Raised circular structure is truncated by channel, interpreted as fluvial channel based partly on network structure not visible in this subframe. Subtle rim may be present, however structure is convex-up overall. Origin is unclear: one possible alternative to impact is preferential erosion around the margins of spatulate soft-sediment-deformation. → CAND. PSP_07474_1745.

514 **Figure S8.** Maps showing locations of:- definite ancient craters (green); rimmed circular mesas
515 (orange); candidate ancient craters (red - excluded from paleopressure calculations); channels
516 and channel belts (gray shading). In most cases crater rims are only partially preserved.



517

DTM2

